

Electrically Driven and Thermally Tunable Integrated Optical Isolators for Silicon Photonics

Duanni Huang, Paolo Pintus, *Member, IEEE*, Chong Zhang, Yuya Shoji, *Member, IEEE*, Tetsuya Mizumoto, *Fellow, IEEE*, and John E. Bowers, *Fellow, IEEE*

Abstract—Optical isolators are required to block undesired reflections in many photonic integrated circuits (PICs), but the performance of on-chip isolators using the magneto-optic effect has been limited due to high loss of such materials. Moreover, they require precise positioning of a permanent magnet close to the chip, increasing footprint and impeding packaging. In this paper, we propose an optical isolator on the silicon-on-insulator platform with record performance and without the use of any external permanent magnets. A metallic microstrip above the bonded silicon microring (MR) is used to generate the magnetic field required for the nonreciprocal behavior. Simultaneously, the microstrip can be used to provide 0.6 nm of thermal tuning while preserving over 20 dB of isolation. We measure 32 dB of isolation near 1555 nm with only 2.3 dB excess loss in a 35 μm radius MR. The tunability, compactness, and lack of permanent magnets suggest this device is a major step towards integration in PICs.

Index Terms—Magneto-optics, optical isolator, ring resonator, photonic integrated circuit, silicon photonics.

I. INTRODUCTION

OPTICAL isolators and circulators are devices that possess the unique capability of breaking symmetry in the propagation of light. More specifically, they possess an asymmetric scattering matrix and break Lorentz reciprocity [1]. The primary approach to achieve nonreciprocity on chip has been to integrate magneto-optic (MO) materials with large Faraday rotation alongside traditional waveguiding materials such as silicon in order to obtain an asymmetric permittivity tensor [2], [13]–[21]. An alternative technique without magnetic materials

involves electro-optic modulation to introduce time-dependent effects, but the observed isolation has been small [3]–[7] or the insertion loss is intrinsically large [8]. A third approach using optical nonlinearity such as the Kerr effect [9] has recently been under scrutiny as it does not always provide isolation when forward and backward propagating light are simultaneously passing through the device [10]. There are some exceptions to this, such as devices based on stimulated Brillouin scattering [11]–[12].

In this paper, we will focus on the MO approach using cerium substituted yttrium iron garnet (Ce:YIG) integrated with silicon waveguides. When a MO waveguide is placed in a magnetic field, the resulting nonreciprocal phase shift (NRPS) can be utilized in an unbalanced Mach-Zehnder interferometer (MZI) [13]–[18] or a microring (MR) [19]–[21] to achieve optical isolation. MZI isolators have demonstrated over 30 dB of isolation as well as large bandwidth, but their excess loss are high due to large footprint and high losses in Ce:YIG (~ 60 dB/cm). MR isolators are much more compact, meaning they can have lower loss. However previous experimental work has showed an isolation smaller than 19.5 dB and, due to their narrow bandwidth, the MR isolators are limited to a specific wavelength.

Moreover, a drawback of both MZI and MR isolators to date has been the use of a permanent magnet to generate a static magnetic field, which is unattractive for integration on chip and impedes packaging. In this work, we eliminate the need of a permanent magnet by using a metal microstrip to directly generate the magnetic field above a bonded Ce:YIG/Si MR isolator. In this work, we also propose to use the same deposited metal for thermal tuning of the MR isolator, allowing for the alignment of the isolation wavelength, which is a critical issue for the implementation of a narrowband device. This can correct for fabrication errors as well as compensate for varying ambient temperatures. Finally, the small footprint of the device keeps the excess loss small. A summary of demonstrated integrated isolators using Ce:YIG on silicon is shown in Fig. 1, including the results achieved in this work. In this figure, we plot the isolation ratio of the device versus the excess loss to the silicon waveguide of previous devices. All of these devices fundamentally operate for TM mode. TM isolators have been integrated with a TE-TM polarization rotator [18] for operation in TE mode.

II. DESIGN AND SIMULATION

The device is an all pass MR filter with 35 μm radius. The Ce:YIG is bonded on a silicon-on-insulator (SOI) MR that is critically coupled to a straight bus waveguide for maximum extinction ratio [22]. When a radially outward magnetic field

Manuscript received January 30, 2016; revised April 30, 2016; accepted July 1, 2016. Date of publication July 7, 2016; date of current version September 12, 2016. D. Huang and P. Pintus contributed equally to this work. This work was supported by the Air Force SBIR under Contract FA8650-15-M-1920 with Morton Photonics, the “Center for Scientific Computing at UCSB” and under NSF Grant CNS-0960316. The work of D. Huang was supported by National Science Foundation Graduate Research Fellowship Program.

D. Huang, C. Zhang, and J. E. Bowers are with the Department of Electrical and Computer Engineering, University of California, Santa Barbara, CA 93106 USA (e-mail: duanni@ece.ucsb.edu; czhang@ece.ucsb.edu; bowers@ece.ucsb.edu).

P. Pintus is with the Department of Electrical and Computer Engineering, University of California, Santa Barbara, CA 93106 USA and also with TeCIP Institute, Scuola Superiore Sant’Anna Pisa 56124, Italy (e-mail: p.pintus@sssip.it).

Y. Shoji is with the Quantum Nanoelectronics Research Center, Tokyo Institute of Technology, Tokyo 152-8552, Japan (e-mail: shoji.y.ad@m.titech.ac.jp).

T. Mizumoto is with the Department of Electrical and Electronic Engineering, Tokyo Institute of Technology, Tokyo 152-8552, Japan (e-mail: tmizumot@pe.titech.ac.jp).

Color versions of one or more of the figures in this paper are available online at <http://ieeexplore.ieee.org>.

Digital Object Identifier 10.1109/JSTQE.2016.2588778

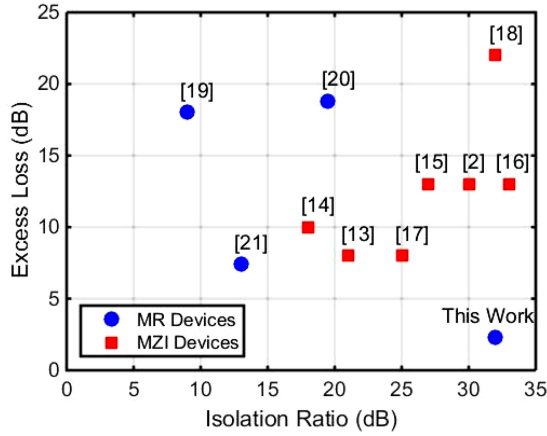


Fig. 1. Comparison of integrated Ce:YIG based isolators on silicon. Our result showing 32 dB of isolation with 2.3 dB of excess loss is shown in the bottom right. The devices in [20] and [21] are fabricated with pulsed-laser deposition of polycrystalline Ce:YIG, while all the others involve wafer bonding of single crystalline Ce:YIG.

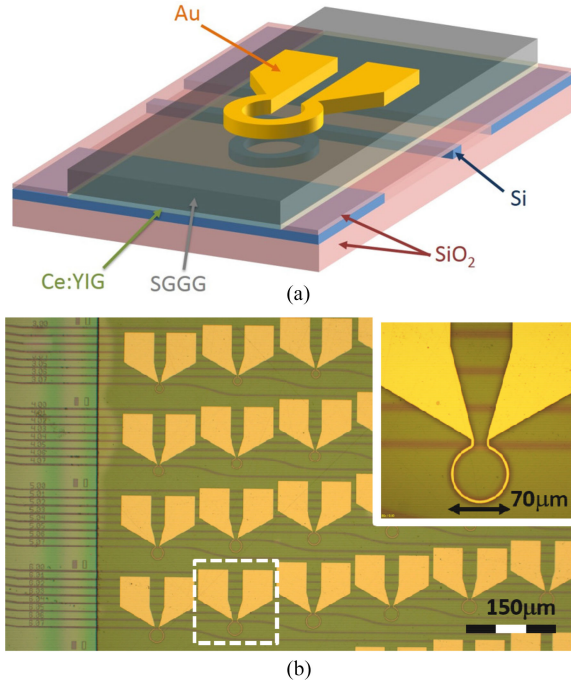


Fig. 2. (Top) Perspective view of the isolator. (b) Microscope image of the fabricated chip, with splits for various microring geometries. The inset shows a close-up of one of the fabricated isolators.

is applied to the MR, the propagation constants of the clockwise (CW) and counterclockwise (CCW) transverse magnetic (TM) modes are differentiated. The resulting NRPS splits the resonances of the CW mode and the CCW mode. When the operating wavelength of the laser is aligned to one of the resonances, then isolation is achieved for the TM mode. A schematic as well as a microscope image of the device is shown below in Fig. 2(a) and (b), respectively.

A. Nonreciprocal Waveguide Analysis

The nonreciprocal behavior of the Ce:YIG/Si waveguide is analyzed using an accurate nonreciprocal mode solver based

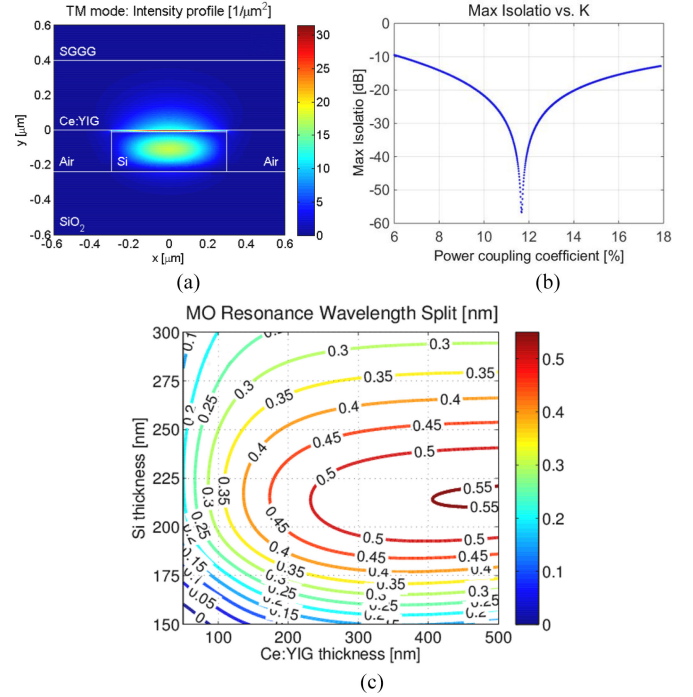


Fig. 3. (a) The cross-section mode profile, in which a silica layer of 10 nm is assumed between the silicon microring and the bonded Ce:YIG layer. (b) The resonance wavelength split for the TM mode with respect to Si and Ce:YIG layer thicknesses. A waveguide width of 600 nm is assumed. (c) A simulation depicting the maximum theoretical isolation for different coupling ratios into the microring.

on the finite element method [22], [23]. Due to the relatively large MR radius, we consider an equivalent straight waveguide to compute the modes and the optical effective index. Both the MR and the bus waveguide are made of silicon (refractive index $n_{Si} = 3.44$) with an air cladding ($n_{Air} = 1$). A Ce:YIG layer ($n_{CeYIG} = 2.22$), which was previously grown on a (Ca, Mg, Zr)-substituted gadolinium gallium garnet (SGGG, $n_{SGGG} = 1.97$) substrate, is bonded over the silicon layer. SGGG is the preferred native substrate for Ce:YIG due to lattice matching. All materials are low loss at $\lambda = 1550$ nm, with the exception of the Ce:YIG which has a propagation loss of about 60 dB/cm, included in the mode analysis. The resonance wavelength split (RWS) between the CW and the CCW mode due to the MO garnet is computed as in Eq. (1) where Δn_{eff} is the effective index variation and n_g is the average group index with respect to the two directions computed at room temperature. The RWS $\Delta\lambda_{MO}$ is also proportional to the Faraday rotation θ_F

$$\Delta\lambda_{MO} = \lambda \frac{\Delta n_{eff}}{n_g}. \quad (1)$$

The cross-section of the waveguide is designed to maximize the RWS, while preserving the single mode TM operation. In the optimal structure, the center of the mode is located near the boundary between the Ce:YIG and the Si, as shown in Fig. 3(a) for the CW mode. In reality, there is a thin layer of SiO₂ at this boundary, due to O₂ surface activation prior to the bonding [24], [25], which can degrade the NRPS for even a thin 10 nm layer

of SiO₂ which is assumed in the computation. Considering a Faraday rotation of Ce:YIG equal to -4500 deg/cm at room temperature (i.e., $T = 20$ °C), the RWS has been evaluated.

The maximum RWS is obtained for a 215 nm thick by 600 nm wide silicon waveguide, and a 400 nm thick Ce:YIG layer. For those values, the maximum of the field is located close to the Ce:YIG/SiO₂/Si interfaces. For this reason, a large bend radius (i.e., 35 μm) and a thicker silicon waveguide are preferred (i.e., 230 nm) in order to keep the mode better confined and reduce the bending loss. Our simulations predict that for a 400 nm thick layer of Ce:YIG bonded to a 230 nm tall by 600 nm wide Si waveguide with 10 nm oxide layer, the nonreciprocal RWS reaches the maximum value of 0.52 nm, as shown in Fig. 3(b).

For the proposed device, the critical power coupling coefficient K is about 11.68%, which corresponds to a gap of about 245 nm. The critical coupling condition is crucial for MR-based systems because it is related to the MR-waveguide distance, which is difficult to be experimentally controlled with high accuracy. Due to the large propagation loss in the Ce:YIG, the coupling condition is less strict and a variation up to 15% from the optimum gap can still guarantee an isolation higher than 20 dB, as shown in Fig. 3(c).

B. Electromagnet Design

To provide the radially outward/inward magnetic field at the ring-Ce:YIG interface, we apply a current through the microstrip, which closely follows the shape of the ring resonator. Since the microstrip is patterned on the back of the bonded Ce:YIG die, it is important to know the thickness of the SGGG substrate. The strength of the magnetic field in the ring is inversely proportional to the distance between the ring and the microstrip (i.e. thickness of SGGG substrate). In our simulations as well as our actual device, we target a thickness of 5 μm . Such a layer is sufficiently thin that an applied current in the microstrip generates a strong magnetic field at the Ce:YIG/SiO₂/Si interface, which induces in-plane magnetization in the Ce:YIG and cause a significant RWS. However, the SGGG is thick enough to avoid optical loss due to overlap between the optical mode and the metallic microstrip. We computed the radial magnetic field using COMSOL Multiphysics, as shown in Fig. 4.

C. Thermal Performance

When the current is applied to the microstrip, it causes a local heating in the MR due to the Joule effect. This induces a thermal resonance wavelength shift as well as a change in the Faraday rotation. We compute the local temperature distribution in the device using COMSOL, as shown in Fig. 5.

By performing the modal analysis of the ring with respect to the temperature, the thermal resonance wavelength shift $\Delta\lambda_T$ is valued as

$$\Delta\lambda_T = \frac{\lambda}{n_g} \left(\sum_i \frac{\partial n_{eff}}{\partial n_i} \frac{\partial n_i}{\partial T} \right) \Delta T \quad (2)$$

where the derivative $\partial n_i / \partial T$ depends on the materials with refractive index n_i , while $\partial n_{eff} / \partial n_i$ can be computed from the

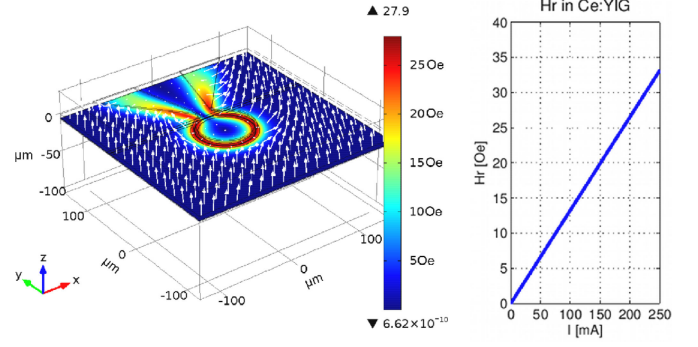


Fig. 4. Simulation of the external magnetic field generated by the electric current in the metal microstrip. The 3D plot shows the intensity of the radial magnetic field in the Ce:YIG plane assuming 200 mA DC current. On the same plot, the arrows indicate the direction of the magnetic field. In the plot on the right, the radial component of the field with respect to the ring (denoted by the bold arrow) as a function of the DC current in the spiral is reported.

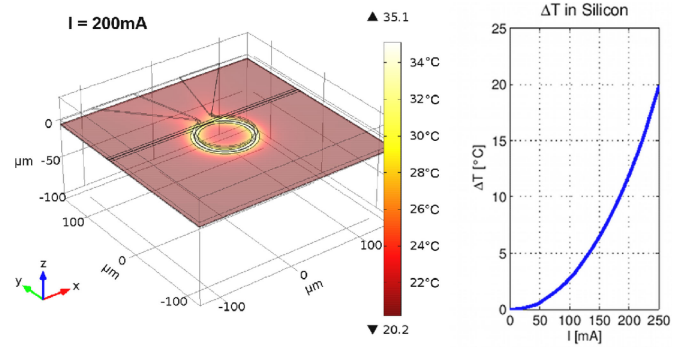


Fig. 5. Simulation of the temperature distribution generated by the electrical current. The 3D plot shows the temperature distribution in the silicon plane assuming 200 mA DC current. In the same plot, the streamlines show the current flux in the spiral. In the plot on the right, the increment of the average temperature in the silicon microring is reported as a function of the DC current in the spiral.

TABLE I
MODAL TEMPERATURE DEPENDENCE

Material	$\partial n_i / \partial T$ [1/°C]	$\partial n_{eff} / \partial n_i$
Ce:YIG	$9.1 \cdot 10^{-5}$	0.405
Si	$1.86 \cdot 10^{-4}$	0.691
SiO ₂	$1.0 \cdot 10^{-5}$	0.275
Air	$1.0 \cdot 10^{-6}$	0.021

The temperature dependence of the material refractive index (middle column) as well as the effect on the modal index (right column).

mode solver [23]. The results of this analysis are summarized in the table below.

For the device under investigation, we calculate a resonance wavelength shift of 0.0716 nm/°C for the TM mode. Due to the temperature variation, θ_F decreases [26] so the MO RWS is

$$\Delta\lambda_{MO}(H_r, T) = \frac{\Delta\lambda_{MO}^0}{\theta_F^0} \cdot \left[\theta_F(H_r) + \frac{d\theta_F}{dT} \cdot \Delta T \right] \quad (3)$$

where $\theta_F^0 = -4500$ °/cm and $\Delta\lambda_{MO}^0$ is the corresponding RWS at room temperature. As the device heats up, the Faraday rotation

will change by $d\theta_F/dT = +44$ degrees/ $^{\circ}\text{C}$ [26]. Combining these two effects, we find that the total resonance wavelength shift is

$$\Delta\lambda = \Delta\lambda_T(T) \pm \frac{1}{2}\Delta\lambda_{MO}(H_r, T) \quad (4)$$

where \pm refer to the CW and CCW modes, respectively.

III. DEVICE FABRICATION

A bare SOI wafer with 500 nm thick Si device layer and 1 μm buried oxide was thinned to 230 nm using dry oxidation at 1050 $^{\circ}\text{C}$ and subsequent buffered HF etch. The wafer was then patterned using 248 nm DUV lithography, and dry etched using a Bosch process to form the waveguides and resonators. Splits were fabricated with varying MR radius as well as coupling gap. In preparation for wafer bonding, both the SOI and the Ce:YIG/SGGG sample are rigorously cleaned, and activated with O_2 plasma. The Ce:YIG is directly bonded onto the SOI patterns, and then annealed at 200 $^{\circ}\text{C}$ for 6 hours under 3 MPa of pressure to strengthen the bond. After the bond, a 1 μm layer of SiO_2 is sputtered everywhere on the chip as an upper cladding. Next, the SGGG substrate is thinned by mounting the sample against a flat chuck, and polishing using a series of increasingly fine lapping films. The thickness of the SGGG is monitored using a micrometer and confirmed to be ~ 5 μm with a separate measurement. Variation of thickness across the sample is roughly 1–2 μm due to imperfect leveling of the chuck. The patterns for the metal microstrip and contact are defined on the backside of the SGGG, and then 22 nm of Ti is deposited as an underlayer, followed by 1.5 μm of Au using electron-beam evaporation. Aluminum can also be used as a CMOS compatible metal with low resistance. The metal microstrips and contacts are released with a lift-off procedure. Finally, the sample is diced and the facets are polished. All the fabrication steps are schematically shown in Fig. 6.

IV. RESULTS AND ANALYSIS

A. Faraday Rotation Measurements

The Faraday rotation of the Ce:YIG is measured by detecting the polarization rotation of light as it passes through a thin film of Ce:YIG on SGGG sample and it is shown in Fig. 7(a) [27]. In this experiment, the direction of propagation as well as the direction of magnetization is out of plane with respect to the sample. The slight decrease after the saturation is due to rotation in the SGGG substrate (paramagnetic). Since the modal overlap with SGGG is negligible, this does not affect the performance of the device. To extract the correct value of the Faraday rotation of the Ce:YIG, we remove the contribution of the SGGG by linear fitting the slope for $|H| > 2.0$ KOe. The processed experimental results are then fit to a hyperbolic tangent function as well as a moving average, showing good agreement in Fig. 7(b).

It is worth noting that the magnetization in Fig. 4 is in-plane, as opposed to the out-of-plane magnetization that was measured in the Fig. 7. While the Faraday rotation constant is the same for both configurations (-4500 deg/cm), the in-plane configuration is called the easy axis of magnetization and only ~ 50 Oe is

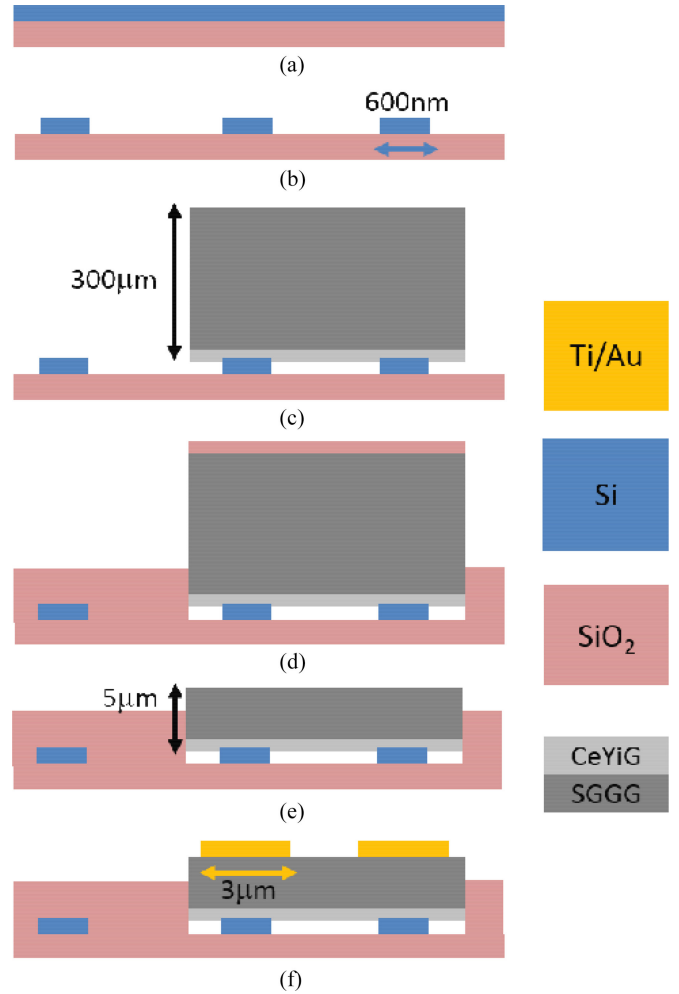


Fig. 6. Process flow beginning with (a) 230 nm thick SOI wafer that is (b) patterned to form waveguides. (c) Ce:YIG/SGGG is bonded. (d) SiO_2 is deposited. (e) Mechanical polishing to thin SGGG substrate. (f) Contact and microstrip deposition on the backside of the SGGG.

required to saturate the Ce:YIG. On the other hand, ~ 3 kOe is needed for saturate the Ce:YIG in the perpendicular direction, i.e., the hard axis of the garnet.

For the device under test, below saturation (50 Oe), θ_F varies linearly with respect to H , like in the measurement shown in Fig. 7. Based on the simulations in Fig. 4, we are in this linear regime for currents smaller than 250 mA. Magnetic hysteresis is also an effect that may be present below saturation, but it has a negligible effect in the device under test, as we later show.

B. Device Characterization

The optical characterization was carried out at room temperature (20 $^{\circ}\text{C}$) on a temperature controlled stage. A polarization maintaining lensed fiber with 2.5 μm spot size was securely clamped in a fiber rotator and rotated to a TM polarization. We measure a polarization extinction ratio of 26 dB. The PM fiber is used to couple light into the device while a SMF is used to couple light out of the device through the polished edge facets. A tunable laser and power sensor is used to scan the transmission spectra from 1500 nm to 1570 nm to observe the intrinsic

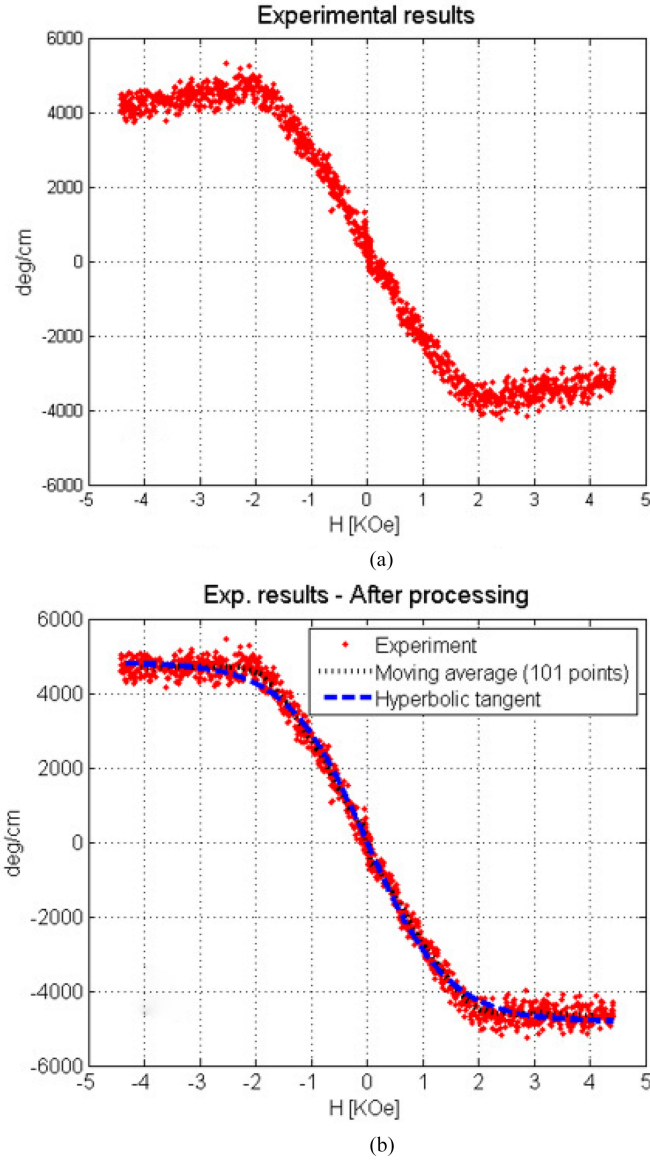


Fig. 7. Faraday rotation with respect to magnetic field applied in the hard axis (out of plane). The results are shown (a) pre and (b) post data processing.

MR spectra. For more isolation measurements, a finer step of 0.1 pm was used to observe the split of a single resonance.

The current was applied using a through beryllium copper probes, and swept from 0 to 220 mA. Applying currents higher than 250 mA resulted in permanent damage to the microstrip due to heating. At each current value, we switch from positive to negative current to measure the RWS while maintaining the same temperature. Switching the direction of the external magnetic field is equivalent to switching the propagation direction of light. This is experimentally verified in the appendix. We then calculate the thermally induced shift by taking the average resonance wavelength of the two spectra, and comparing that to the spectrum of the MR when the zero current is applied. By comparing the spectra with positive and negative applied current, optical nonreciprocity and isolation can be evaluated.

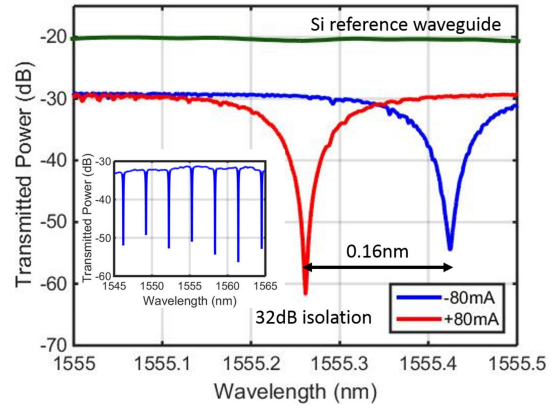


Fig. 8. Spectrum measurement at $I = \pm 80$ mA. The inset shows the intrinsic spectrum of the microring over multiple free spectral ranges without any applied current.

C. Measured isolation

The two transmission spectra are shown in Fig. 8 when ± 80 mA of current is applied, for which we measure 32 dB of isolation. The electrical power used by the isolator was 9.6 mW when accounting for the measured 1.5Ω resistance of the microstrip. The optical loss of the device is measured by comparing our device to a straight Si reference waveguide of the same dimensions, but without the bonded Ce:YIG. Of the 10 dB loss, we simulate 1.2 dB of scattering loss at the interfaces between the channel waveguide with a silica cladding and the Ce:YIG bonded waveguide using Lumerical FDTD software. The remaining 8.8 dB is due to absorption in the Ce:YIG layer. Since the length of the bus (3.5 mm) is much longer than the isolator ($70 \mu\text{m}$ diameter) due to placement of splits on the mask as seen in Fig. 2, there are the equivalent length of eight isolators, including the microstrip and contacts, along the bus waveguide. Therefore, the excess loss of a single isolator is $(1.2 + 8.8/8) = 2.3$ dB. The excess loss can be further reduced by considering silicon nitride cladding ($n = 2$) in place of silicon dioxide due to a smaller refractive index contrast with the Ce:YIG ($n = 2.22$), and smaller mode mismatch at the lateral bonded interface.

The MO RWS between CW and CCW propagation is 0.16 nm, which suggests that while the magnetization of the Ce:YIG is not saturated for 80 mA of current, it is more than enough for high isolation. This is in contrast to previously demonstrated isolators, in which the magnetization is always saturated due to the use of a strong permanent magnet. Since the MR is narrowband, any resonance split larger than 0.1 nm will result in an isolation that is equal to the full extinction ratio of the MR, as is the case here. Therefore, a strong magnet and full saturation of the Ce:YIG magnetization is not needed for optical isolation. The device has a 10 dB bandwidth of 1.2 GHz, meaning over 22 dB of isolation is achieved in this range. This is significantly wider than semiconductor laser linewidths [28]. In externally modulated laser (EML) applications, the isolator can be integrated between the laser and modulator. For direct modulation applications, modulation induced sidebands

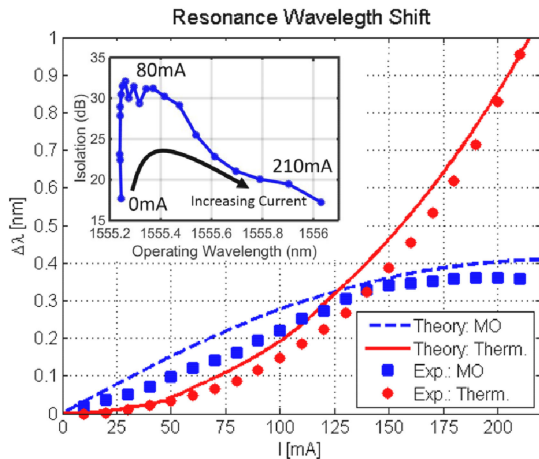


Fig. 9. The MO split and the thermal shift are shown with respect to the electrical current. Theoretical and experimental values are compared. In the inset, the optical isolation is reported over the full tuning range. Since the resonance wavelength initially shifts to shorter wavelengths at small currents, the curve appears to double back on itself with increasing current.

may not be isolated although they are not synchronous with the carrier signal, which lessens their effect on RIN degradation.

D. Thermal Tuning

This microstrip approach also allows us to thermally tune the operating wavelength by applying different amounts of current. As we sweep the current from 0 to 220 mA, we can observe both the nonreciprocal wavelength split (MO split), as well as the reciprocal thermally induced redshift (Therm. shift) of the resonances. From the data, the MO wavelength split saturates at a value of 0.36 nm, which is lower than the originally predicted 0.52 nm in Fig. 3(b) due to the temperature dependence of Faraday rotation [26]. Taking into account the Joule heating effect, we obtain a very good agreement between the experimental and simulated results, as proved in Fig. 9. The tunability is shown in the inset in which we demonstrate 0.6 nm of tuning while maintaining over 20 dB of isolation, which is limited by deviation from critical coupling and damage to the microstrip at high currents. In our device, the thermal and magnetic effects are inherently coupled because there is only one microstrip and Faraday rotation is temperature dependent. Therefore, thermal tuning also results in changing the nonreciprocal RWS. Reducing the coupling between the two effects by using additional heater pads could result in higher efficiency, wider tuning ranges, and optimized control of the thermal tuning.

Hysteresis was not observed to play a strong effect in the tuning, as shown in Fig. 10. We imitate a hysteresis sweep by increasing the current from 0 to 210 mA (blue), back to 0 mA (red), down to -210 mA (green), and finally back to 0 mA (black). We do this in 10 mA intervals, with roughly one minute between each measurement to allow temperatures to reach steady state. When we plot the resonance wavelength of the ring, we see that the data is consistent across the whole sweep. The plot is not symmetric because it includes both thermal and MO effects. For positive current, the thermal effect causes redshift while the

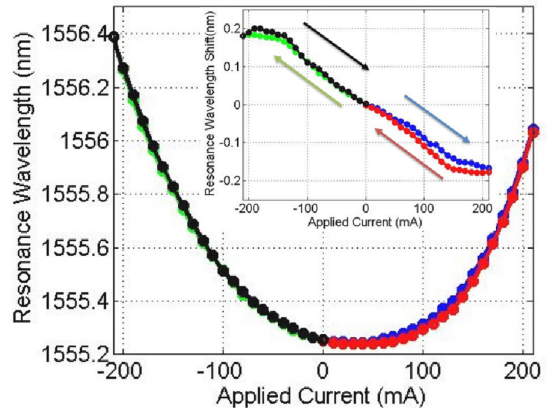


Fig. 10. A measurement of the resonance wavelength as the current is swept back and forth, similar to a hysteresis loop measurement. The inset shows the nonreciprocal wavelength split from MO effect.

MO effect causes blueshift. For negative current, both effects cause redshift.

The inset shows the nonreciprocal wavelength split. There appears to be no noticeable residual magnetization in the material, as shown by the fact that the resonance frequency when no current is applied is the same at the beginning and the end of this measurement. There is some difference at higher currents (~ 0.03 nm), which could be attributed to some thermal instability at the higher temperature.

Overall, hysteresis is weak because the magnetic fields do not fully saturate the magnetization in the garnet. Furthermore, by switching between positive and negative currents, we are consistently switching the magnetization in the material. We believe this has a demagnetization effect on the material, which limits its hysteresis behavior.

V. CONCLUSION

In conclusion, we have demonstrated a compact integrated optical isolator on SOI with 32 dB of isolation for the TM mode, 2.3 dB of excess loss to silicon and 0.6 nm of wavelength tuning using a current induced MO effect that consumes 9.6 mW of power. This novel method does not require a permanent magnet and instead utilizes a deposited gold microstrip for thermal tuning as well as a source for magnetic fields. We also present a model that accurately predicts the thermal, magnetic, and optical effects and interactions within the device. The device architecture can be further improved by thinning the SGGG substrate even further for lower power consumption or selectively removing the Ce:YIG on the bus waveguide to decrease loss. We believe that the dynamic control of magnetic fields in precise configurations on chip in this approach can also be utilized in other MO devices such as MZI isolators, circulators, switches, modulators, and sensors.

APPENDIX

The direction of the magnetic field applied is always given relative to the propagation direction of light. In normal operation of an isolator, the propagation direction is reversed, while the

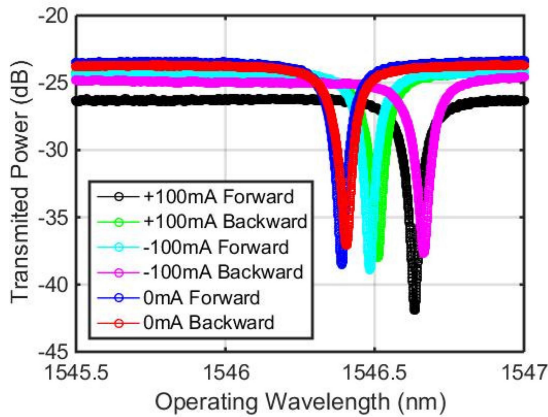


Fig. 11. The spectrum of the isolator for forward and backward propagating light under different current bias.

magnetic field is unchanged. This effect can also be observed vice versa, in which we switch the direction of the magnetic field (current) without changing the propagation direction, as the effects are mathematically equivalent. We verify this in our device experimentally by manually switching the propagation direction of light by changing which fiber is used as input. We expect to see that this has the same effect as switching the magnetic field. In practice, it is difficult to maintain the exact same polarization at the end of the two fibers. The results are shown in Fig. 11 for an applied current of 100 mA. In this case, the isolator was not near critical coupling so the extinction ratio and isolation are not as large. Nevertheless, it is evident that +100 mA with forward optical propagation is roughly equivalent to -100 mA with backward propagation. Similarly, +100 mA with backward optical propagation is very close to -100 mA in the forward direction. The resonance split is clearly seen in both cases and verifies the nonreciprocity in the device. The slight error in the measurement can be attributed to not achieving identical coupling conditions for forwards and backwards propagation with regard to polarization. This is apparent from noticing the difference between the forward and backward spectra without any applied current.

ACKNOWLEDGMENT

The authors would like to thank P. Morton, J. Khurgin, J. Peters, D. Spencer, M. Davenport, L. Chang, T. Komljenovic, and F. Di Pasquale for helpful discussions.

REFERENCES

- [1] D. Jalas *et al.*, "What is—and what is not—an optical isolator," *Nature Photon.*, vol. 7, no. 8, pp. 579–582, 2013.
- [2] Y. Shoji and T. Mizumoto, "Magneto-optical non-reciprocal devices in silicon photonics," *Sci. Technol. Adv. Mater.*, vol. 15, no. 1, 2014, Art. no. 014602.
- [3] Z. Yu and S. Fan, "Complete optical isolation created by indirect interband photonic transitions," *Nature Photon.*, vol. 3, no. 2, pp. 91–94, 2009.
- [4] C. Doerr, L. Chen, and D. Vermeulen, "Silicon photonics broadband modulation-based isolator," *Opt. Express*, vol. 22, no. 4, pp. 4493–4498, 2014.
- [5] H. Lira, Z. Yu, S. Fan, and M. Lipson, "Electrically driven nonreciprocity induced by interband photonic transition on a silicon chip," *Phys. Rev. Lett.*, vol. 109, no. 3, 2012, Art. no. 033901.
- [6] L. Tzuang, K. Fang, P. Nussenzeig, S. Fan, and M. Lipson, "Non-reciprocal phase shift induced by an effective magnetic flux for light," *Nature Photon.*, vol. 8, no. 9, pp. 701–705, 2014.
- [7] M. Heck, S. Srinivasan, M. Davenport, and J. Bowers, "Integrated microwave photonic isolators: Theory, experimental realization and application in a unidirectional ring mode-locked laser diode," *Photonics*, vol. 2, no. 3, pp. 957–968, 2015.
- [8] S. Bhandare *et al.*, "Novel nonmagnetic 30-dB traveling-wave single-sideband optical isolator integrated in III/V material," *IEEE J. Sel. Topics Quantum Electron.*, vol. 11, no. 2, pp. 417–421, Mar./Apr. 2005.
- [9] L. Fan *et al.*, "An all-silicon passive optical diode," *Science*, vol. 335, no. 6067, pp. 447–450, 2011.
- [10] Y. Shi, Z. Yu, and S. Fan, "Limitations of nonlinear optical isolators due to dynamic reciprocity," *Nature Photon.*, vol. 9, no. 6, pp. 388–392, 2015.
- [11] C. Dong *et al.*, "Brillouin-scattering-induced transparency and non-reciprocal light storage," *Nature Commun.*, vol. 6, 2015, Art. no. 6193.
- [12] C. Poulton *et al.*, "Design for broadband on-chip isolator using stimulated Brillouin scattering in dispersion-engineered chalcogenide waveguides," *Opt. Express*, vol. 20, no. 19, pp. 21235–21246, 2012.
- [13] Y. Shoji, T. Mizumoto, H. Yokoi, I. Hsieh, and R. Osgood, "Magneto-optical isolator with silicon waveguides fabricated by direct bonding," *Appl. Phys. Lett.*, vol. 92, no. 7, 2008, Art. no. 071117.
- [14] Y. Shoji, M. Ito, Y. Shirato, and T. Mizumoto, "MZI optical isolator with Si-wire waveguides by surface-activated direct bonding," *Opt. Express*, vol. 20, no. 16, pp. 18440–18448, 2012.
- [15] Y. Shoji, Y. Shirato, and T. Mizumoto, "Silicon mach-zehnder interferometer optical isolator having 8 nm bandwidth for over 20 dB isolation," *Jpn. J. Appl. Phys.*, vol. 53, no. 2, 2014, Art. no. 022202.
- [16] Y. Shoji, K. Miura, and T. Mizumoto, "Optical nonreciprocal devices based on magneto-optical phase shift in silicon photonics," *J. Opt.*, vol. 18, no. 1, 2015, Art. no. 013001.
- [17] S. Ghosh *et al.*, "Ce:YIG/silicon-on-insulator waveguide optical isolator realized by adhesive bonding," *Opt. Express*, vol. 20, no. 2, pp. 1839–1848, 2012.
- [18] S. Ghosh *et al.*, "Optical isolator for TE polarized light realized by adhesive bonding of Ce:YIG on silicon-on-insulator waveguide circuits," *IEEE Photon. J.*, vol. 5, no. 3, Jun. 2013, Art. no. 6601108.
- [19] M. Tien, T. Mizumoto, P. Pintus, H. Kromer, and J. E. Bowers, "Silicon ring isolators with bonded nonreciprocal magneto-optic garnets," *Opt. Express*, vol. 19, no. 12, pp. 11740–11745, 2011.
- [20] L. Bi *et al.*, "On-chip optical isolation in monolithically integrated non-reciprocal optical resonators," *Nature Photon.*, vol. 5, no. 12, pp. 758–762, 2011.
- [21] X. Sun *et al.*, "Single-step deposition of cerium-substituted yttrium iron garnet for monolithic on-chip optical isolation," *ACS Photon.*, vol. 2, no. 7, pp. 856–863, 2015.
- [22] P. Pintus, M. Tien, and J. E. Bowers, "Design of magneto-optical ring isolator on SOI based on the finite-element method," *IEEE Photon. Technol. Lett.*, vol. 23, no. 22, pp. 1670–1672, Nov. 2011.
- [23] P. Pintus, "Accurate vectorial finite element mode solver for magneto-optic and anisotropic waveguides," *Opt. Express*, vol. 22, no. 13, pp. 15737–15756, 2014.
- [24] Y. Liu *et al.*, "Growth of ultrathin SiO₂ on Si by surface irradiation with an O₂⁺ Ar electron cyclotron resonance microwave plasma at low temperatures," *J. Appl. Phys.*, vol. 85, no. 3, pp. 1911–1915, 1999.
- [25] D. Liang, G. Roelkens, R. Baets, and J. E. Bowers, "Hybrid integrated platforms for silicon photonics," *Materials*, vol. 3, no. 3, pp. 1782–1802, 2010.
- [26] K. Furuya, K. Kato, Y. Shoji, and T. Mizumoto, "Demonstration of an athermal waveguide optical isolator on silicon platform," in *Proc. Eur. Conf. Opt. Commun.*, 2015, pp. 1–3.
- [27] T. Shintaku, U. Takehiko, and M. Kobayashi, "Magneto-optic channel waveguides in Ce-substituted yttrium iron garnet," *J. Appl. Phys.* vol. 74, no. 8, pp. 4877–4881, 1993.
- [28] L. Coldren, S. Corzine, and M. Masanovic, *Diode Lasers and Photonic Integrated Circuits*, vol. 218. New York, NY, USA: Wiley, 2012.

Duanni Huang received the B.S. degree in electrical engineering from the Massachusetts Institute of Technology, Cambridge, MA, USA, in 2013. He received the M.S. degree in electrical engineering from the University of California, Santa Barbara, CA, USA, in 2015, where he is currently working toward the Ph.D. degree. His current research interests include the field of silicon photonics, with an emphasis on magneto-optic and other nonreciprocal phenomenon.

Paolo Pintus (S'10–M'11) was born in Cagliari, Italy, in 1983. He received the Bachelor's degree (Hons.) and the Master's degree (Hons.) in electronic engineering from the University of Cagliari, Cagliari, Italy, in 2005 and 2007, respectively, and the Ph.D. degree in innovative technologies of ICT and robotics from the Scuola Superiore Sant'Anna, Pisa, Italy, in 2012. In 2007, he was a Visiting Student (Leonardo da Vinci program) in the Department of Biological Sciences, Imperial College of London, London, U.K. From 2010 to 2011, he was a Visiting Researcher and in 2015, he was a Visiting Assistant Project Scientist with the Optoelectronics Research Group, University of California Santa Barbara, Santa Barbara, CA, USA.

He is currently a Research Fellow at Scuola Superiore Sant'Anna, Pisa, Italy, and a Member of the National Inter-University Consortium for Telecommunications. His research interests include the field of integrated optics, silicon photonics, and numerical method for electromagnetism.

Chong Zhang received the B.S. degree in electrical science and technology from the Harbin Institute of Technology, Harbin, China, in 2007, and the M.S. degree in optical engineering from Zhejiang University, Hangzhou, China, in 2010. He is currently working toward the Ph.D. degree at the University of California, Santa Barbara, CA, USA. His research interests include epitaxial growth of III/V materials on silicon, photonics integration devices on hybrid silicon platform, and applications for high-speed optical interconnection.

Yuya Shoji (M'09) received the B.E., M.E., and Ph.D. degrees in electrical engineering from the Tokyo Institute of Technology, Tokyo, Japan, in 2003, 2005, and 2008, respectively. He was a Postdoctoral Fellow with the National Institute of Advanced Industrial Science and Technology, Tsukuba, Japan, from 2008 to 2010. He has been an Assistant Professor with the Graduate School of Science and Engineering, Tokyo Institute of Technology, from 2011 to 2014. He is currently an Associate Professor with the Quantum Nanoelectronics Research Center, Tokyo Institute of Technology. His current research interests include device designs and fabrication of magneto-optical devices, silicon nanophotonic devices, and the photonic integrated circuits. He is a Member of the Optical Society of America, The Institute of Electronics, Information and Communication Engineers, the Japan Society of Applied Physics, and the Magnetic Society of Japan.

Tetsuya Mizumoto (S'81–M'84–F'12) received the B.E., M.E., and D.Eng. degrees in electrical engineering from the Tokyo Institute of Technology, Tokyo, Japan, in 1979, 1981, and 1984, respectively. He has been a Research Assistant at the Tokyo Institute of Technology since 1984. He is currently a Professor with the Graduate School of Science and Engineering, Tokyo Institute of Technology. His current research interests include waveguide optical devices, especially magneto-optic devices.

Dr. Mizumoto received the Treatise Award in 1994 and the Best Letter Award of Electronics Society Transactions in 2007 from the Institute of Electronics, Information and Communication Engineers (IEICE). He received the IEEE Photonics Society Distinguished Lecturer Award in July 2009, IEEE Fellow grade for "Contributions to investigations of waveguide optical nonreciprocal devices for optical communications" in January 2012, and IEICE Achievement Award for "Pioneering work on optical nonreciprocal circuits" in May 2012. He is a Fellow of IEICE and a Member of the Japan Society of Applied Physics and the Magnetic Society of Japan.

John E. Bowers (F'93) received the M.S. and Ph.D. degrees from Stanford University, Stanford, CA, USA. He holds the Fred Kavli Chair in Nanotechnology, and is the Director of the Institute for Energy Efficiency and a Professor in the Department of Electrical and Computer Engineering and Materials, University of California, Santa Barbara (UCSB). He is a Cofounder of Aurion, Aerius Photonics and Calient Networks. He worked for AT& Bell Laboratories and Honeywell before joining UCSB. He is a Member of the National Academy of Engineering and a Fellow of the IEEE, OSA, and the American Physical Society. He received the OSA/IEEE Tyndall Award, the OSA Holonyak Prize, the IEEE LEOS William Streifer Award, and the South Coast Business and Technology Entrepreneur of the Year Award. He and coworkers received the EE Times Annual Creativity in Electronics Award for Most Promising Technology for the heterogeneous silicon laser in 2007. His research interests primarily include optoelectronics and photonic integrated circuits. He has published 10 book chapters, 600 journal papers, and 900 conference papers and has received 54 patents.